Published in final edited form as:

Proc SPIE Int Soc Opt Eng. 2017 ; 10066: . doi:10.1117/12.2255843.

Preliminary Assessment of a Hysteroscopic Fallopian Tube Heat and Biomaterial Technology for Permanent Female Sterilization

Prajan Divakar[1], **B. Stuart Trembly**[1], **Karen L. Moodie**[2], **P. Jack Hoopes**[1,2], **Ulrike G.K. Wegst**[1]

[1]Thayer School of Engineering, Dartmouth College, Hanover, NH 03755, USA

[2]Geisel School of Medicine, Dartmouth College, Hanover, NH 03755, USA

Abstract

Recent failures in hysteroscopic female sterilization procedures have brought into question the implantation of non-resorbable metal devices into the fallopian tubes due to long-term risks such as migration, fragmentation, and tubal perforation. The goal of this study is to assess whether a porous, biodegradable implant can be deposited into the fallopian tube lumen with or without a local mild heat treatment to generate a safe and permanent fallopian tube occlusion/sterilization event. The technologies investigated included freeze-cast collagen-based scaffolds and magnetic nanoparticle (MNP) based scaffolds. *In vitro* assessment of iron oxide MNP-based scaffolds was performed to determine the absorption rate density (ARD); subsequent computational modeling quantified the thermal *in vivo* steady state temperature as a function of tubal radius for treatment planning. For collagen-based scaffolds, *in vivo* testing was performed to study the biocompatibility in a mouse flank model, followed by implantation into an *in vivo* anestrus feline uterine horn (animal model for the fallopian tube). Biological responses were studied histopathologically. Uterine horn patency was assessed via radiographic imaging. Preliminary studies suggest the MNP-impregnated scaffold and a safe, noninvasive AMF excitation field have potential to generate a sufficient focal fallopian tube thermal dose to create a fibrotic healing event and ultimately, permanent tubal occlusion.

Keywords

tissue scaffold; freeze casting; magnetic nanoparticles; tubal occlusion; uterine horn

1. INTRODUCTION

In 2015, more than 400 million married or in-union women globally, used contraception to prevent unintended pregnancy; of these, more than 200 million utilized female sterilization as their method of choice.[1] Currently, the only hysteroscopic, non-surgical, option to achieve permanent sterilization is the Essure® procedure, whereby a nickel-titanium (nitinol) coil with an inner stainless steel coil coated with polyethylene terephthalate (PET) fibers is transcatheterally guided through the cervix and deposited into each fallopian tube. Durable scar tissue occlusion of the tubes is confirmed after three months through a hysterosalpingogram, whereby radiopaque dye is transcervically injected into the uterus under x-ray imaging.[2] While largely successful after more than 750,000 implantations

worldwide, recent reports have revealed thousands of Essure® failures in patients that are associated with device migration, fragmentation, and/or perforation through tissue.[3,4] Subsequent FDA scrutiny has called into question the fundamental safety of the Essure® procedure.[5,6]

We address these challenges with a new biomaterial-based solution. Previous experimental and commercial technologies,[3,7] have indicated that heating is an attractive method to de-epithelialize the fallopian tube and promote fibrosis and tubal occlusion. However, drawbacks such as feedline heating of surrounding tissue, incomplete occlusion, and/or the presence of an associated non-biodegradable foreign body have not yet been overcome. An attractive method that previously had not been studied for this application is the use of magnetic nanoparticles (MNPs) for heating that have successfully been used for cancer treatment.[8] In an alternating magnetic field, MNPs generate heat, with which a thermal dose can be applied that may be adequate for female sterilization. A key experimental challenge, however, is the localization and containment of MNPs for activation in a well-defined treatment zone. Freeze-cast biomaterial scaffolds are highly porous, have a high surface area, and possess a hierarchical structure, inviting and promoting cell/tissue integration while maintaining structural integrity and can be custom-designed for a given application through control of material composition, chemical bonding, and fabrication parameters.[9–13] By incorporating MNPs into freeze-cast scaffold, biomaterials can be made that can be activated remotely to de-epithelialize and damage the intramural portion of the fallopian tube to cause fibrotic tubal occlusion. As an alternative approach, bare collagen-based scaffolds were assessed *in vivo* to explore their potential as a standalone device that can be partially or fully resorbable. In both cases, the scaffolds are designed to overcome current medical device limitations.

Described in this paper are both MNP-based scaffolds and the *in vitro* evaluation of their potential as heatable biomaterials and the *in vivo* testing of bare scaffolds to understand their biocompatibility and biological responses in the mouse flank and feline uterine horn (animal model for the human fallopian tube).

2. MATERIALS AND METHODS

2.1 Scaffold Material Compositions

MNP-based scaffolds were made from a slurry composed of aqueous suspensions of 1% w/v cellulose nanofibril (CNF) in water (University of Maine, Orono, Maine) that were thoroughly mixed with a known mass of freeze-dried dextran-coated iron oxide nanoparticles (micromod Partikeltechnologie GmbH, Rostock, Germany) under the name bionized nanoferrite (~100 nm diameter) to achieve concentrations of 25 mg Fe/mL or 250 mg Fe/mL (as measured by dividing the known mass of Fe contained in the measured scaffold volume). Bare scaffolds were made from a slurry of 1% w/v bovine tendon collagen (Worthington Biochemical Corporation, Lakewood, NJ) and 1% w/v nanocellulose blend of Bioplus™ nanocellulose fibrils and crystals (American Process, Atlanta, GA) mixed in a 50:50 v/v ratio.

2.2 Scaffold Freeze casting and Lyopholization

Slurries were deposited via needle and syringe ($16^{1/2}$ gauge) in 4 mm diameter, 45 mm long cylindrical bores in a cylindrical aluminum mold. The bottom of the mold was sealed with a removable Teflon™ cap. After loading the material of interest and equilibrating it to room temperature, the bottom of the mold was placed on a copper coldfinger, which is cooled by liquid nitrogen and whose temperature at the mold bottom is controlled through heating with a bandheater and PID controller. A cooling rate of 10°C/min was applied to the mold until a temperature of −150°C was reached. After the slurries were frozen, the samples were gently punched out from the mold manually and placed in a lyopholizer at room temperature (22°C) and 0.008 mBar for 36 hours to remove the ice phase by sublimation.

2.3 Scaffold Crosslinking

For crosslinking, the lyophilozed collagen-nanocellulose scaffolds were fully submersed and gently stirred for 6 hours at room temperature in 200 proof ethanol with 33 mM 1-Ethyl-3-(3-dimethylaminopropyl) carbodiimide and 6 mM N-hydroxysuccinimide (Sigma-Aldrich, St. Louis, MO). To wash the scaffolds and remove excess crosslinking agents, they were then submersed and stirred three times in distilled water for 2 hours, 12 hours, and 1 hour, respectively. Lastly, the wet crosslinked scaffolds were flash frozen in liquid nitrogen and lyophilized.

2.4 Structural Characterization

Scanning electron microscopy (SEM) was used to analyze scaffold microstructure. All SEM images were acquired with the Tescan VEGA 3 scanning electron microscope (Tescan, Brno, Czech Republic) and software and processed with ImageJ.[14]

2.5 MNP-based Scaffold Characterization

The specific heat (C_p) of the raw materials was measured with a Netzsch DSC 200 F3 differential scanning calorimeter (NETZSCH-Gerätebau GmbH, Selb, Germany). The specific heat of the raw material was determined with sapphire as the reference sample using the expression:[15]

$$\frac{cp}{cp'} = \left(\frac{y}{y'}\right)\left(\frac{m'}{m}\right) \quad \text{Equation 1}$$

where c_p is the specific heat, y the heat flow differential, m the mass, and the prime symbol indicates the reference material parameters.

With the specific heat values for the components either determined experimentally or provided by literature, the mixture specific heat for each scaffold was determined with an expression of the Kopp-Neumann Law:[16]

$$cp_{mixed} = \frac{\sum_{i=1}^{n} m_i cp_i}{\sum_{i=1}^{n} m_i} \quad \text{Equation 2}$$

Where m_i is the mass and c_{pi} is the specific heat of the components.

2.6 MNP-based Scaffold Activation and ARD

A custom designed circular copper coil connected to a current generator was used to generate an alternating magnetic field (AMF). For testing, 30 μL of distilled water were added to the 5 mm cylindrical scaffolds to mimic *in vivo* water content. Subsequent scaffold activation at multiple AMF strengths was measured in Oersted (Oe) at a constant field frequency of 169 kHz and visualized with a forward looking infrared (FLIR) camera.

To determine heating performance in an AMF, the scaffolds were imaged with a FLIR camera (SC300 Series, FLIR Instruments, Boston, MA) and processed with the eXamine IR software provided by FLIR Instruments. The circular cross-section of the scaffolds was visualized to quantify the change in temperature (°C) with respect to time (seconds), or dT/dt. The heating profile data illustrating temperature versus time was fit to a quadratic function, and the goodness of fit was measured with the coefficient of determination (r^2). The rate of temperature change dT/dt was then evaluated at time equals zero. The absorption rate density (ARD) in Watts per mL was calculated for the scaffolds, utilizing the scaffold's values for dT/dt, density (g/mL), and composite specific heat [J/(g.°C)].[17]

$$ARD = \rho Cp_{mixed} \frac{dT}{dt} \quad \text{Equation 3}$$

where ARD is the absorption rate density, ρ is the density, c_{pmixed} is the composite specific heat, and dT/dt is the rate of temperature change.

2.7. MNP-based Scaffold Computational Model

Given the experimentally determined ARD, the steady-state solution 1-D Bioheat equation in cylindrical coordinates was used to mathematically model with MATLAB R2016B software (The Mathworks Inc., Natick, MA) steady-state temperature as a function of radial location[18,19] within the intramural fallopian tube/feline uterine horn in the presence of a MNP-based scaffold of a certain internal radius:

$$T = \frac{\sqrt{\frac{k}{B}}}{Ak} \frac{Q}{K_1\left(\sqrt{\frac{B}{K}} r_0\right)} K_0\left(\sqrt{\frac{B}{k}} r\right) + 37^{\circ}C \quad \text{Equation 4}$$

where T is the steady state temperature (°C), r_0 is the internal radius (mm), A is the outside surface area of heated portion (m^2), B is the blood perfusion term in mL/(min.100g) with a

conversion factor of $6\times;10^{-7}$ included to give Watts/(°C.mm^3), k is the thermal conductivity (Watts/(mm.°C)), Q is the total absorbed power (Watts), K_1 is the first order modified Bessel function of the second kind, and K_0 is the zero order modified Bessel function of the second kind.

A heat treatment length (L) of 35 mm and an internal radius of 2 mm (the radial boundary constraint) were chosen to match the MNP-based scaffold dimensions that were fabricated. The area (A) was determined by calculating the cylindrical surface area with r_0 and L. Blood perfusion was assumed to be 10 mL/(min.100g) and converted to Watts/(°C.mm^3) and thermal conductivity was 0.0005 Watts/(mm.°C) as informed by literature.[20] Experimental work performed with anestrus feline uterine horns suggests that there are two key anatomical regions in this animal model: i) a central mucosal region (approximate radius of 1- 1.5 mm) made of elastic connective tissue lined with a columnar epithelial monolayer and ii) two surrounding and concentric muscle layers (approximately 1 millimeter thick in total) that provide transverse and longitudinal support, respectively. With the insertion of a 2 mm radius scaffold, we suspect that the uterine horn will dilate mildly to accommodate the implant. We approximate the dilated connective tissue and muscle layers to be approximately 2.5 mm and 3.5 mm, respectively, from the center of the scaffold. Lastly, the total absorbed power (Q) was calculated by multiplying the experimentally determined ARD by the cylindrical scaffold volume with r_0 and L.

To assess a potential thermal dosage time at given temperature in a select region of the uterine horn that is higher than 43°C we can leverage the widely used cumulative equivalent minutes formula at 43°C:[21]

$$CEM43 = 0.5^{(43-T)}t \quad \text{Equation 5}$$

where $CEM43$ is the cumulative equivalent minutes at 43 °C, T is the dosage temperature, and t is the dosage time at temperature T.

2.8 *In vivo* Collagen-nanocellulose Scaffold Implantation

Bare scaffolds were sectioned appropriately for the respective models (mouse: 6 mm, cat: 15 mm), massed, and sterilized in a sealed container with ethylene oxide gas for approximately 24 hours. All animals in this study were handled as approved by the IACUC and experiments were in compliance with the NIH Guide for Care and Use of Laboratory Animals.

2.8.2 Mouse Biocompatibility—Two to three-month-old mice (21-22 grams) were under study. The lower body of the mice was shaved prior to surgery. All mice received analgesia prior to surgery and were anesthetized under vaporized isoflurane. Post-anesthesia, three sequential antiseptic scrubs with chlorohexidine, ethanol, and betadine were performed on every surgical site. A one-centimeter transverse cut and opening was made in either the left or right side of the lower body wall. A tapered rubber catheter loaded with the scaffold was inserted into the surgical pocket. The 6 mm long implant was deposited upon inserting a rubber plunger and retracting the catheter. Proline suture was used to close the incision. The

procedure was performed bilaterally. Analgesia was administered less than 24 hours post-surgery. Sutures were removed 7 days post-surgery. Animals were sacrificed 15 days post-surgery. All animals were fixed in 10% formalin post-sacrifice for at least 24 hours. The left and right body wall sections in each mouse containing the implants were resected with surgical scissors. The body wall samples were mildly stained and preserved in eosin and paraffin, respectively. Each processed body wall sample was sectioned transversely, blocked in paraffin, thinly sliced under microtome, and stained with hematoxylin and eosin for transmission light microscopy with an Olympus BX50 transmission light microscope (Olympus Corporation, Tokyo, Japan).

2.8.2 Feline Case Study—A three and half month female feline was under study. The lower abdomen was shaved prior to surgery and blood was drawn and spun down for 1 mL of serum. Post-anesthesia and analgesia, a midline laparotomy was performed to expose the uterine horns. A centimeter longitudinal incision was made in the uterine body. A 15 mm collagen-based scaffold was soaked in feline serum and a sterile blunt stainless steel introducer was used to forward the scaffold into place in the uterine horn. Proline suture was used to close the horn, followed by subcutaneous closure of the abdomen with PDS and surgical glue. Post-operative monitoring and analgesia was performed. After 35 days following the biomaterial implantation, a midline laparotomy was performed to inject radiopaque dye into the uterine body under x-ray imaging. Subsequently, an ovariohysterectomy was performed, and the uterine horn was harvested, fixed in formalin, and processed for histology and imaging as described in 2.8.1; the feline was monitored under post-operative care until full recovery, after which she was adopted.

3. RESULTS

The results of this paper are twofold: i) *in vitro* characterization and computational modeling of MNP-based scaffolds and ii) in vivo histopathological assessments of bare scaffolds in the mouse subcutaneous flank and feline uterine horn models. Scanning electron micrographs were obtained for the low (25 mg Fe /mL) and high (250 Fe mg/mL) concentration MNP-based scaffolds to depict both the transverse interior and longitudinal exterior cross sections (Figure 1). These images reveal the porosity and structural features of freeze-cast scaffolds, but also show artifacts from the sample preparation by mechanical cutting with a razor blade.

To determine the absorption rate density of the scaffolds, specific heat values of the individual scaffold components were determined (Table 1). These values of Table 1 were used to calculate the specific heat of the MNP-based scaffolds (Table 2).

The product of the specific heat with the density of the scaffold (Table 2) and heating performance (rate of temperature change with time) in an AMF yield the ARD at a given field strength and frequency (Table 3).

Using the high concentration ARD value under an AMF at 257 Oe and 169 kHz to approximate total absorbed power for a treatment length of 35 mm and scaffold radius of 2

mm, steady-state temperature was plotted as a function of tubal radius (Figure 2). Subsequent CEM43 calculations were performed to predict a viable thermal dose.

For bare scaffold *in vivo* assessment, low and high magnification transverse histopathological sections were taken for both the subcutaneous mouse flank and feline uterine horn to reveal scaffold and tissue responses (Figures 3 and 4).

4. DISCUSSION

This study shows that it is possible to freeze-cast biomaterial scaffolds and successfully integrate iron oxide MNPs, achieving an iron concentration of 250 Fe mg/mL, which is about two and a half times higher than concentrations reported in literature to date.[8] When comparing the 25 mg Fe /mL and 250 mg Fe /mL scaffolds it is apparent that there is a tradeoff between porosity and nanoparticle content (Figure 1). The high concentration scaffolds are denser with lower structural elasticity due to MNP incorporation into the fibrillar nanocellulose structure, a structure which forms a strong and resilient porous network and architecture in the lower concentration scaffold. These results suggest that it is feasible and attractive to achieve similarly high Fe concentration scaffolds with biodegradable biopolymers, such as collagen or related materials and composites, instead of nanocellulose.

By testing the heating properties of the MNP-enabled scaffolds at multiple field strengths, the low iron concentration scaffolds with 25 mg Fe /mL were found to start heating at about 300 Oe with a dT/dt of 0.0967 °C/sec, while the high iron concentration scaffolds with 250 mg Fe /m already heated at only half the field strength with a dT/dt of the same order (Table 3). To assess whether this performance is clinically applicable *in vivo* with the adequate thermal dose, we used the experimentally determined ARD of the high concentration scaffold of 1.447 watts/mL at 257 Oe and 169 kHz to determine a power input (Q) for the modified Bessel equation, which solves the bioheat equation for a cylinder (Equation 4). Based on the steady state temperature equation as a function of radius, we computationally modelled the MNP-based scaffold in the tubal lumen. We estimated that the steady state temperature in the mucosa is 46°C (Figure 2). Previous research has indicated that a thermal treatment must completely kill the epithelial and damage mucosal connective tissue sufficiently to promote fibrotic healing without severely compromising surrounding muscle layers and vasculature (Hoopes & Trembly, unpublished). Using cumulative equivalent minutes at 43°C as a metric for thermal dosimetry (Equation 5), a CEM43 greater than 80 is likely required to damage the cells *in vivo* in the mucosal region of interest.[22] For our estimation, we chose a CEM43 of 200; this equates to a thermal dose in the mucosa of 46°C for 25 minutes. While it is unclear whether this dose is sufficient to allow for fibrotic healing and occlusion, there are still future improvements that may result in a fundamentally more efficient treatment plan. Certain MNPs have been shown to heat with an ARD eight times higher than that of MNPs that were similar to those used in this study.[23] Such a drastic difference in performance could result in a greatly increased steady state temperature and a correspondingly reduced heating time to achieve the desired dose.

Given our focus on the development of a biomaterial implant, we also chose to assess the use of a scaffold alone in the absence of thermal de-epithelialization. First, our two-week biocompatibility study using collagen-nanocellulose scaffolds revealed a characteristic fibro-granulomatous encapsulation (Figure 3), which included fibroblasts, macrophages, and neutrophils. We hypothesize that with longer implantation time, fibrous encapsulation will occur coupled with fibroblast infiltration into the collagen scaffold, resulting in its resorption until degraded, leaving behind trace amounts of fully integrated non-toxic nanocellulose nanofibrils.

Translating the information from the murine histology, we addressed the question of implantation into the uterine horn. We wanted to assess the scaffold's performance without heat and thus in the presence of a functional epithelium. Histology taken after 35 days (Figure 4) revealed the presence of compacted nanocellulose with minimal collagen in the lumen of the uterine horn. The shape of some scaffold fragments closely mimicked the internal lumen contour, suggesting that the implant may have been dehydrated during processing (Figure 4); this may explain the partial occlusion that was noted under x-ray imaging upon injection of radiopaque dye in the implant region. The presence of fluid may also be indicative of mucosal fibrosis, the result of an inflammatory pathway in reaction to the foreign body that is unlikely to progress to permanent occlusion. Another key finding was the phagocytic degradation in the connective tissue interior to the epithelium lining the tubal lumen, of what appeared to be collagen from the scaffold (Figure 4). In the absence of any fibrous encapsulation, we conclude that the presence of the epithelium during the initial healing period is an obstacle to the permanent fibrotic occlusive outcome we are targeting.

5. CONCLUSION

In this paper, we present the successful fabrication of a porous, biodegradable implant made both without and with a high concentration of iron oxide MNPs for deposition into the fallopian tube lumen with or without a mild local heat treatment, respectively, to generate safe and permanent fallopian tube occlusion and sterilization. To assess the applicability of such a device for female sterilization, we computationally modeled the fallopian tube/uterine horn, based on the bioheat equation for cylindrical tissue, to predict the steady state temperature that would be subsequently used to plan a thermal dose. Our model suggests that the MNP-based scaffold approach can generate a steady state temperature, which in combination with adequate heating time, will provide a thermal dose capable of safely damaging cells and initiating healing. Currently, it is unclear what thermal dose is required to promote an occlusive scar healing response. Future research will determine, which thermal dose will achieve the desired outcome and at the same time be high enough to prevent functional regeneration and low enough to avoid an overheated injury that may heal incompletely.

Our investigation of the bare collagen-based scaffolds suggested that the implant is biocompatible and encapsulated in fibrous tissue in the presence of connective tissue, such as the subcutaneous mouse flank. Using this information and based on conventional epithelial damage pathophysiology, we hypothesize that the direct association of the scaffold with a de-epithelialized mucosa will facilitate the occlusive healing response we desire. We

further hypothesize that fibroblasts, neutrophils, and macrophages from the underlying de-epithelialized mucosa will behave in a manner similar to the displayed subcutaneous mouse flank scaffold encapsulation reaction. Further experiments will be performed to explore these hypotheses and also whether tissue encapsulation or tissue integration are preferable to achieve the goal of safe and permanent fallopian tube occlusion and sterilization.

ACKNOWLEDGMENTS

The authors would like to thank the Thayer and Dartmouth College Electron Microscopy facilities, the Center for Comparative Medicine and Research, and the Dartmouth Hitchcock Medical Center for expert advice and resources and gratefully acknowledge research support through NIH-NICHD Grant No. 5R21HD087828-02. The authors also thank James D. Petryk, Dr. Alicia A. Petryk, and Isabella Caruso for their contribution.

REFERENCES

[1]. United Nations, Department of Economic and Social Affairs. “Population Division Trends in Contraception Use Worldwide 2015,” (ST/ESA/SER.A/349) (2015).

[2]. Veersema S “Hysteroscopy and contraception,” Best Practice & Research Clinical Obstetrics & Gynaecology, 29(7), 940–950 (2015). [PubMed: 26013880]

[3]. la Chapelle CF, Veersema S, Brölmann HA, & Jansen FW “Effectiveness and feasibility of hysteroscopic sterilization techniques: a systematic review and meta-analysis,” Fertility and sterility, 103(6), 1516–1525 (2015). [PubMed: 25910565]

[4]. Palmer SN, & Greenberg JA “Transcervical sterilization: a comparison of Essure® permanent birth control system and Adiana® permanent contraception system,” Rev Obstet Gynecol, 2(2), 84–92 (2009) [PubMed: 19609402]

[5]. Rabin R “Long Term Data on Complications Adds to Criticism of Contraceptive Implant,” New York Times. 5–7 (2015).

[6]. Rabin R “Bayer’s Essure Contraceptive Implant, Now With a Warning,” New York Times. D6 (2016).

[7]. Trembly BS, Manganiello PD, & Hoopes PJ “Microwave occlusion of the rabbit uterine horn,” BiOS’98 International Biomedical Optics Symposium (pp. 50–60). International Society for Optics and Photonics (1998).

[8]. Maier-Hauff K, Ulrich F, Nestler D, Niehoff H, Wust P, Thiesen B, Orawa H, Budach V, & Jordan A “Efficacy and safety of intratumoral thermotherapy using magnetic iron-oxide nanoparticles combined with external beam radiotherapy on patients with recurrent glioblastoma multiforme,” Journal of neuro-oncology, 103(2), 317–324 (2011). [PubMed: 20845061]

[9]. Deville S “Freeze-casting of porous biomaterials: structure, properties and opportunities,” Materials, 3(3), 1913–1927 (2010).

[10]. Hunger PM, Donius AE, & Wegst UGK “Structure-property-processing correlations in freeze-cast composite scaffolds,” Acta biomaterialia, 9(5), 6338–6348 (2013). [PubMed: 23321303]

[11]. Riblett BW, Francis NL, Wheatley MA, & Wegst UGK “Ice-templated scaffolds with micro-ridged pores direct DRG neurite growth,” Advanced Functional Materials, 22(23), 4920–4923 (2012).

[12]. Wegst UGK, Schecter M, Donius AE, & Hunger PM “Biomaterials by freeze casting,” Philosophical Transactions of the Royal Society of London A: Mathematical, Physical and Engineering Sciences, 368(1917), 2099–2121 (2010).

[13]. Wegst UGK, Hao B, Saiz E, Tomsia AP, & Ritchie RO “Bioinspired structural materials,” Nature Materials, 14, 23–36 (2015). [PubMed: 25344782]

[14]. Rasband WS “ImageJ,” U. S. National Institutes of Health, Bethesda, Maryland, USA, http://imagej.nih.gov/ij/, (2016).

[15]. O’neill MJ “Measurement of Specific Heat Functions by Differential Scanning Calorimetry,” Analytical Chemistry, 38(10), 1331–1336 (1966).

[16]. Inaba H & Naito K “Heat capacity of nonstoichiometric compounds,” Japan Society of Calorimetry and Thermal Analysis. 4(1), 10–18 (1977).

[17]. Wong TZ, Strohbehn JW, Jones KM, Mechling JA, & Trembly BS “SAR patterns from an interstitial microwave antenna-array hyperthermia system,” IEEE transactions on microwave theory and techniques, 34(5), 560–567 (1986).

[18]. Pennes HH “Analysis of tissue and arterial blood temperatures in the resting human forearm,” Journal of applied physiology, 1(2), 93–122 (1948). [PubMed: 18887578]

[19]. Atkinson WJ, Brezovich IA, & Chakraborty DP “Usable frequencies in hyperthermia with thermal seeds,” IEEE Transactions on Biomedical Engineering, (1), 70–75 (1984). [PubMed: 6724612]

[20]. Strohbehn JW, Trembly BS, & Douple EB “Blood flow effects on the temperature distributions from an invasive microwave antenna array used in cancer therapy,” IEEE Transactions on Biomedical Engineering, (9), 649–661 (1982). [PubMed: 7129469]

[21]. Sapareto SA, & Dewey WC “Thermal dose determination in cancer therapy,” International Journal of Radiation Oncology* Biology* Physics, 10(6), 787–800 (1984).

[22]. Dewhirst MW, Viglianti BL, Lora-Michiels M, Hanson M, & Hoopes PJ “Basic principles of thermal dosimetry and thermal thresholds for tissue damage from hyperthermia,” International Journal of Hyperthermia, 19(3), 267–294 (2003). [PubMed: 12745972]

[23]. Shubitidze F, Kekalo K, Stigliano R, & Baker I “Magnetic nanoparticles with high specific absorption rate of electromagnetic energy at low field strength for hyperthermia therapy,” Journal of applied physics, 117(9), 094302 (2015). [PubMed: 25825545]

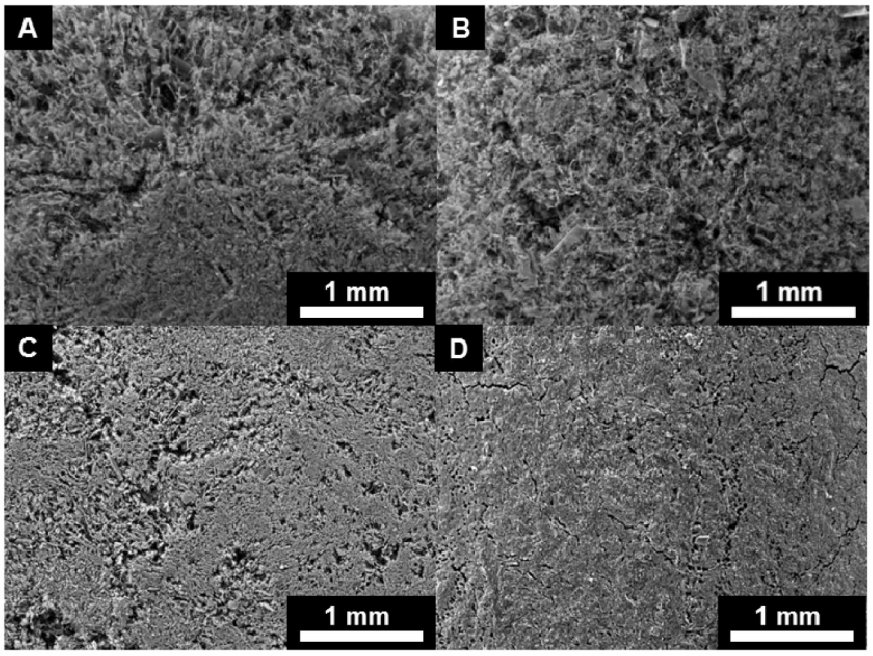

Figure 1:

25 mg Fe/mL CNF scaffold radial interior (A) and longitudinal exterior (B) SEM sections; 250 mg Fe/mL CNF scaffold radial interior (C) and longitudinal exterior (D) SEM sections.

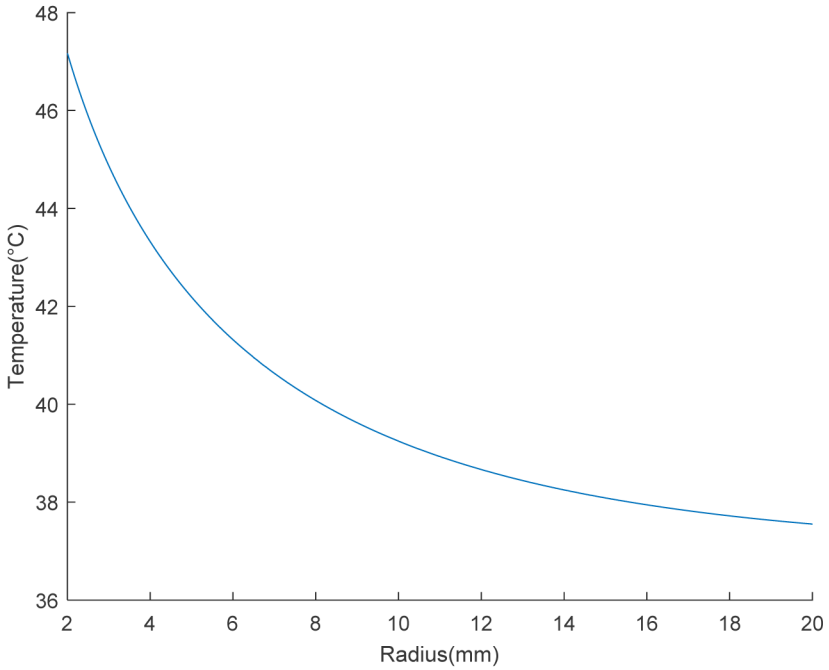

Figure 2:

Steady state temperature as a function of radius for an MNP-based scaffold treatment in the tubal lumen; the radius of 2 mm marks the radial boundary constraint.

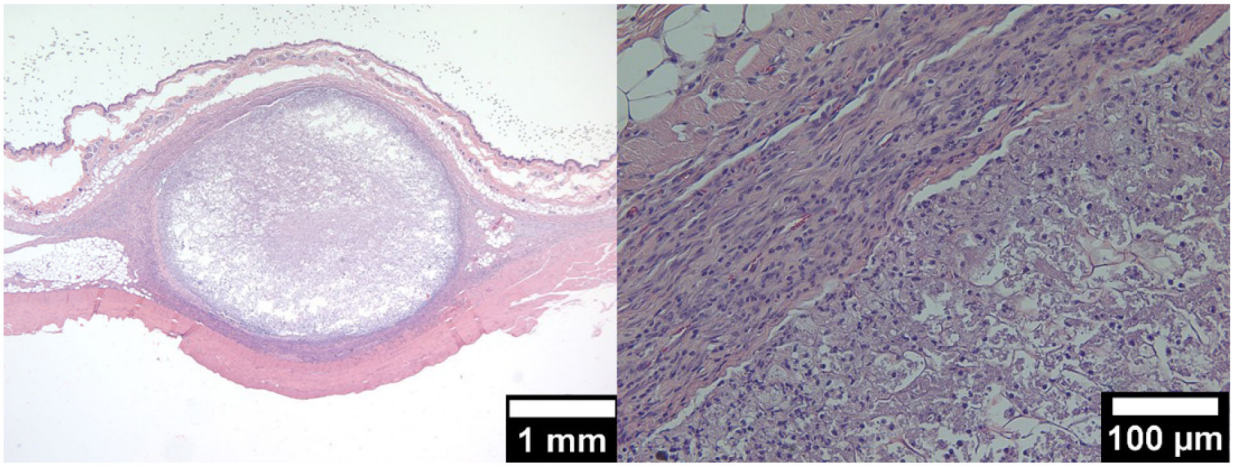

Figure 3:
Transverse section of a crosslinked collagen-nanocellulose scaffold in the subcutaneous mouse flank; low magnification (left); high magnification (right).

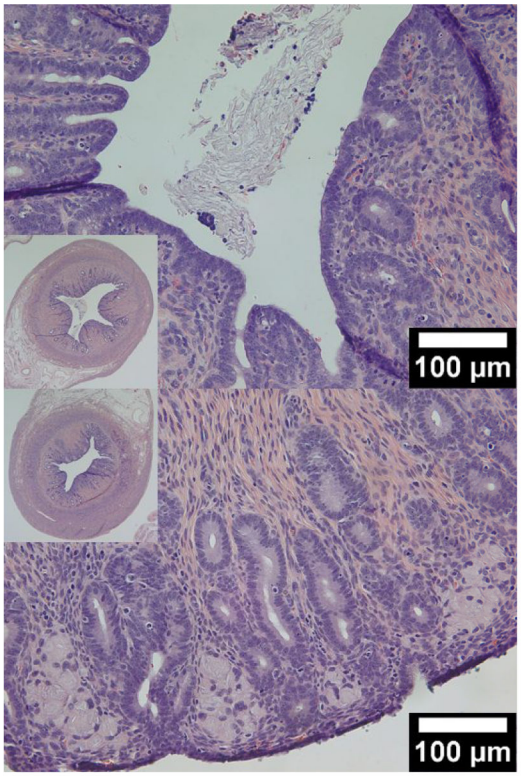

Figure 4:
Transverse sections of the feline uterine horn with the residual collagen-nanocellulose scaffold 35 days post-implantation; compacted scaffold in the lumen (top); phagocytic giant cell clusters underneath the epithelium in the mucosa (bottom).

Table 1:

MNP-based Scaffold Component Specific Heat

Biomaterial:	c_p: [J/(g.°C)]
CNF	1.959
MNP	0.552
Water	4.186

Table 2:

MNP-based Scaffold Specific Heat and Density

[Fe]:(mg/mL)	25	250
Scaffold Biomaterial:	CNF	CNF
c_{pmixed}: [J/(g.°C)]	3.748	2.345
Density: (g/mL)	0.551	0.979

Table 3:

MNP-based Scaffold Heating Performance

[Fe] (mg/mL)	Scaffold Material	AMF (Oe)	Frequency (kHz)	dT/dt (°C/sec)	r^2	ARD (W/mL)
25	CNF	136	169	0.0409	0.944	0.0846
25	CNF	198	169	0.0808	0.996	0.1670
25	CNF	257	169	0.0499	0.994	0.1031
25	CNF	291	169	0.0967	0.998	0.1999
25	CNF	323	169	0.1110	0.998	0.2294
250	CNF	136	169	0.0713	0.996	0.1637
250	CNF	198	169	0.2486	0.997	0.5707
250	CNF	257	169	0.6303	1.000	1.447